EUROPEAN ORGANIZATION FOR NUCLEAR RESEARCH

OPAL Physics Note PN456
30th August 2000

Measurement of Double-Tagged Events in Two-Photon Collisions at LEP

The OPAL Collaboration

Abstract

The interaction of virtual photons is investigated using the reaction $e^+e^- \to e^+e^-$ hadrons based on data taken by the OPAL experiment at e^+e^- centre-of-mass energies $\sqrt{s_{ee}} = 189 - 202$ GeV. The measured cross-sections are compared to predictions of the Quark Parton Model (QPM), to the Leading Order QCD Monte Carlo model PHOJET, and to BFKL calculations. PHOJET describes the data reasonably well, the QPM predicted cross-section is too low and the cross-section prediction based on a Leading Order BFKL calculation is too large.

This note describes preliminary OPAL results

1 Introduction

The classical way to investigate the structure of the photon at e^+e^- colliders is the measurement of the process

$$e(p_1)e(p_2) \rightarrow e(p_1')e(p_2') \,\text{hadrons}, \tag{1}$$

proceeding via the exchange of two photons, which can be either quasi-real, γ, or virtual $\gamma^\star$. The terms in brackets represent the four-vectors of the particles as shown in Fig. 1.

Depending on the virtualities of the exchanged photons the scattered electrons[1] can be observed in the detector. In the case where none of the electrons is observed (anti-tagged), the structure of the quasi-real photon has been studied by OPAL in terms of total cross-sections [1] and jet production [2]. If only one electron is observed (single-tagged), the process can be described as deep-inelastic electron scattering off a quasi-real photon. These events have been studied by OPAL to measure the QED and QCD photon structure functions [3–6]. If both electrons are observed (double-tagged), the dynamics of highly virtual photon collisions is probed. The QED structure of highly virtual photons has already been studied by OPAL [3]. In the analysis presented here, the investigation of highly virtual photon interactions is extended to the measurement of the hadronic structure of the photon. The results are based on data recorded by the OPAL experiment at LEP in the years 1998 and 1999 at e^+e^- centre-of-mass energies of $\sqrt{s_{ee}} = 189 - 202$ GeV, using events where both scattered electrons are observed in the small-angle silicon-tungsten (SW) luminometer. The measured differential cross-sections are compared to the prediction of the Quark Parton Model (QPM), to the PHOJET Monte Carlo model [7] and to BFKL calculations [8]. A similar analysis has been published by the L3 Collaboration [9].

2 Theoretical framework

In this paper double-tagged events are studied, i.e. both final state electrons are measured, which means they must be scattered at sufficiently large polar angles[2] θ_i. This corresponds to the situation where both radiated photons, which take part in the hard scattering process, are highly virtual. Throughout the paper, $i = 1, 2$ denotes quantities which are connected with the upper and lower vertex in Fig. 1, respectively.

The virtualities of the radiated photons are given by $Q_i^2 = -(p_i - p_i^{'})^2 > 0$. The usual dimensionless variables of deep inelastic scattering are defined as:

$$y_1 = \frac{q_1 q_2}{p_1 q_2}, \qquad y_2 = \frac{q_2 q_1}{p_2 q_1}, \tag{2}$$

[1] Electrons and positrons are generically referred to as electrons.

[2] The right-handed OPAL coordinate system is defined with the z axis pointing in the direction of the e^- beam and the x axis pointing horizontally towards the center of the LEP ring. The polar angle θ, the azimuthal angle ϕ and the radius R are the usual spherical coordinates.

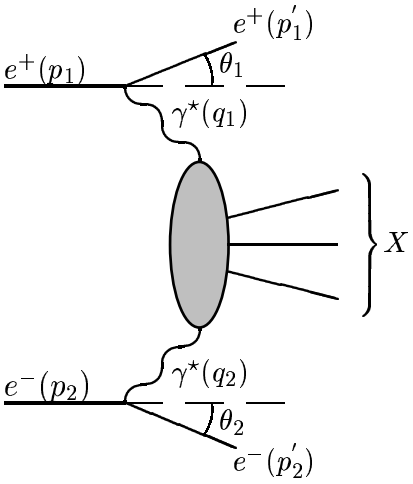

Figure 1: The diagram corresponding to the process $e^+e^- \to e^+e^-$ hadrons.

$$x_1 = \frac{Q_1^2}{2q_1q_2}, \qquad x_2 = \frac{Q_2^2}{2q_2q_1}. \tag{3}$$

The e^+e^- centre-of-mass energy squared is given by $s_{ee} = (p_1 + p_2)^2$ and the hadronic invariant mass squared by $W^2 = (q_1 + q_2)^2$.

The kinematical variables Q_i^2, y_i and x_i are obtained from the four-vectors of the tagged electrons and the hadronic final state via:

$$Q_i^2 = 2E_b E_i(1 - \cos\theta_i), \tag{4}$$

$$y_i = 1 - \frac{E_i}{E_b}\cos^2(\theta_i/2), \tag{5}$$

$$x_i = \frac{Q_i^2}{Q_1^2 + Q_2^2 + W^2}, \tag{6}$$

where E_b refers to the energy of the beam electrons, and the mass m_e of the electron has been neglected.

In this analysis, the hadronic invariant mass, W, is obtained from the energies, E_h, and momenta, $\vec{p}_h$, of final state hadrons (h), excluding the scattered electrons, as follows:

$$W^2 = \left(\sum_h E_h\right)^2 - \left(\sum_h \vec{p}_h\right)^2 = E_{had}^2 - \vec{p}_{had}^{\,2}\,. \tag{7}$$

For the comparison of the data to BFKL calculations the following additional kinematic quantity, which is a measure of the length of the gluon ladder, is defined [10]:

$$Y = \ln\left(\frac{s_{ee}}{s_0}\right) \tag{8}$$

with $s_{\rm ee}/s_0 = s_{\rm ee} y_1 y_2/\sqrt{Q_1^2 Q_2^2} \simeq W^2/\sqrt{Q_1^2 Q_2^2}$, where the last equality requires $W^2 \gg Q_i^2$.

The differential cross-section for the process of Eq. 1 in the limit $Q_i^2 = -q_i^2 \gg m_{\rm e}^2$ and for small values of y_i is given by [11]

$$\begin{aligned} {\rm d}^6\sigma &= \frac{{\rm d}^3{\rm p}_1' {\rm d}^3{\rm p}_2'}{E_1\, E_2}\, \mathcal{L}_{TT} \left(\sigma_{\rm TT} + \sigma_{\rm LT} + \sigma_{\rm TL} + \sigma_{\rm LL} + \frac{1}{2}\tau_{\rm TT} \cos 2\bar{\phi} - 4\tau_{\rm TL} \cos\bar{\phi} \right) \\ &= \frac{{\rm d}^3{\rm p}_1' {\rm d}^3{\rm p}_2'}{E_1\, E_2}\, \mathcal{L}_{TT}\, \sigma_{\gamma^\star\gamma^\star}\,, \qquad L_{\rm TT} = \int \frac{{\rm d}^3{\rm p}_1' {\rm d}^3{\rm p}_2'}{E_1\, E_2} \mathcal{L}_{TT}, \end{aligned} \tag{9}$$

where $\bar{\phi}$ is the angle between the two scattering planes of the electrons in the photon-photon centre-of-mass system. The cross-sections $\sigma_{\rm TT}$, $\sigma_{\rm TL}$, $\sigma_{\rm LT}$ and $\sigma_{\rm LL}$ and the interference terms $\tau_{\rm TT}$ and $\tau_{\rm TL}$ correspond to specific helicity states of the interacting photons (T=transverse and L=longitudinal). The factor $L_{\rm TT}$ describes the flux of transversely polarized photons, and only depends on the four-vectors q_1, q_2, p_1, p_2 and on the mass of the electron [12].

In the case of lepton pair production $\rm e^+e^- \to e^+e^-l^+l^-$ the cross-section is completely determined by QED. However, for hadronic final states QCD corrections have to be taken into account, and the cross-sections and interference terms cannot be completely calculated within the framework of perturbative QCD. For $\mu^+\mu^-$ final states [3] it is found that the contributions from $\tau_{\rm TT}$ and $\tau_{\rm TL}$ are large, for $Q_1^2 \approx Q_2^2$ and small values of W^2. Consequently it cannot be excluded that the interference terms and contributions from longitudinal photons in the QCD case are also large [12]. The cleanest experimental quantity which can be extracted without making further assumptions, e.g. on the interference terms, is the cross-section for the reaction $\rm e^+e^- \to e^+e^-$ hadrons as given in Eq. 9. By dividing with $L_{\rm TT}$ also the cross-section $\sigma_{\gamma^\star\gamma^\star}$ for the reaction $\gamma^\star\gamma^\star \to$ hadrons can be extracted with $\sigma_{\gamma^\star\gamma^\star}$ denoting the sum of all terms contained in the bracket of Eq. 9. Therefore, only comparisons to theoretical models containing predictions for all cross-sections and interference terms are meaningful.

Recently, much attention has been given to the BFKL pomeron [8], especially for small Bjorken-x deep-inelastic electron-proton (ep) scattering at HERA. With increasing centre-of-mass energies squared, s, and for moderate photon virtualities, large logarithms in $1/x$ are expected to dominate the rise of the cross-section. Resummation of these logarithms leads to the so-called BFKL evolution equation from which one derives that the ep cross-section should increase as s^{α_0} with $\alpha_0 \sim 0.5$ in Leading Order (LO), where α_0 denotes the Pomeron intercept. The onset of such BFKL effects has been searched for in ep structure function and hadronic final state data, but the situation is so far inconclusive [13].

It has been argued [10,14–16] that $\rm e^+e^-$ colliders offer an excellent opportunity to test the BFKL prediction, through a measurement of $\sigma_{\gamma^\star\gamma^\star}$. For sufficiently large photon virtualities Q_1^2 and Q_2^2 (a few GeV^2), the BFKL calculation can be carried out without phenomenological input. The leading-log resummation for $\gamma^\star\gamma^\star$ scattering, given by the so-called 'gluon ladder diagrams', is sketched in Fig. 2. The original LO BFKL calculations led to expect an increase of $\sigma_{\gamma^\star\gamma^\star}$ by a factor 20 or more compared to LO BFKL calculations [17]. Meanwhile the LO calculations have been improved by including charm quark mass effects, running of

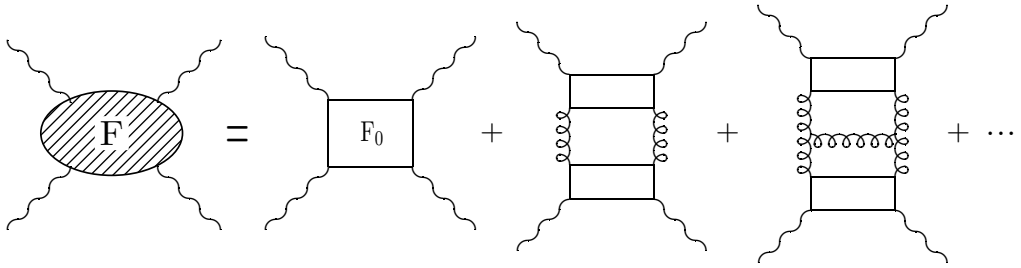

Figure 2: Diagrams contributing to the leading $\ln 1/x$ approximation for the $\gamma^\star\gamma^\star$ cross-section.

the strong coupling constant α_s and the contribution of the longitudinal photon polarisation states. Recently, it has become clear that the Next-to-Leading Order (NLO) corrections to the BFKL equation are large and effectively reduce the value of α_0. A phenomenological determination of the Higher Order (HO) effects was presented in Ref. [16] and the resulting BFKL scattering cross-sections were shown to increase by a factor 2-3 only, relative to the calculations without BFKL effects. Since then theoretically motivated improved higher order calculations have been performed, leading to a range 0.2-0.3 of predicted α_0 values, depending on the renormalisation scheme used.

3 Monte Carlo generators

Several Monte Carlo generators have been compared to the data or used to correct the data for detector effects. Most relevant to the analysis presented here are the programs which are used to model two-photon interactions for double-tagged, single-tagged and anti-tagged events. Here, only the main features of the programs are shortly described. For further details the reader is referred to the original publications. An overview can be found in [12].

The PHOJET1.10 event generator has been used to simulate double-tagged events[3], based on the Dual Parton Model, containing both hard and soft processes [7]. The hard processes are calculated in Leading Order (LO) perturbative QCD, and soft processes are modelled based on γp, pp and p$\bar{\text{p}}$ data assuming Regge factorisation. The $\gamma^*\gamma^*$ cross-section is obtained from the $\gamma\gamma$ cross-section by extrapolating in Q^2 on the basis of the Generalised Vector Dominance model using Ref. [18]. The events are generated for soft as well as hard partonic processes. A cut-off on the transverse momentum of the scattered partons in the photon-photon centre-of-mass system of 2.5 GeV is used to separate the two classes of events. For this reason the generation of events with W below 5 GeV is known to be incomplete. As a cross-check of the PHOJET model the PYTHIA 6.130 [19] Monte Carlo generator, based

[3]There are significant differences between PHOJET1.10 and the previous version PHOJET1.05 in several aspects of the event generation.

on a recent model by Friberg and Sjöstrand [20], is used for the simulation of double-tagged two-photon events.

The general purpose Monte Carlo program HERWIG5.9+$k_{\rm t}$ (dyn) [21] was used to simulate single-tagged two-photon events. This model version uses a modified transverse momentum distribution, $k_{\rm t}$, for the quarks inside the photon, with the upper limit dynamically (dyn) adjusted according to the hardest scale in the event, which is of order Q^2. This has been found [22] to give a better description of the experimentally observed hadronic final states.

The PHOJET1.10 Monte Carlo has also been used to simulate anti-tagged two-photon events. It is known to describe satisfactorily the OPAL anti-tagged two-photon data [1].

The Quark Parton Model QPM cross-section $\rm e^+e^- \to e^+e^-q\overline{q}$, which corresponds to the diagram labelled F_0 in Fig. 2, was calculated with the GALUGA [23] program, which includes all terms from Eq. 9. The quark masses assumed are 0.325 GeV for uds and 1.5 GeV for c quarks. However, for the region of $W > 5$ GeV considered here, the results depend weakly on the assumed quark masses. GALUGA was also used to calculate $L_{\rm TT}$.

Radiative corrections are calculated with the program BDK [24]. As for the GALUGA Monte Carlo, the BDK program calculates the QPM cross-section with, in addition, initial and final state QED radiative corrections to the scattered electrons. It has been verified that the non-radiative cross-sections predicted by BDK and GALUGA agree with each other. GALUGA has more flexibility for calculating cross-sections and is therefore used to calculate the $L_{\rm TT}$ factors and QPM predictions. The size of the radiative corrections depends on the variables used to calculate the kinematics, and also to some extend on the Born cross-section. Fig. 3 compares two methods to calculate the variable Y. The first method uses the hadronic final state variable W. The second method uses y_1 and y_2 calculated from the electrons, if at least one y_i is larger than 0.25, otherwise Y is calculated as for the first method. The QPM Born cross-section was reweighted to the leading order PHOJET cross-section, which agrees well with the measured cross-section (see Section 7). Fig. 3 shows the ratio of the Born to the full radiative (measured) cross-section. For the fully hadronic method the radiative corrections are small. However, for the electron method the corrections can be larger than 50% at large Y values. Obviously, measurements based on the electron kinematics cannot be compared readily with models or BFKL calculations in the region $Y > 4$, unless radiative corrections have been applied. Since the actual size of the radiative corrections also depends on the Born cross-section itself, an iterative procedure would be required to extract the Born cross-section. Since the present statistics does not permit such a procedure, only the hadronic variables have been used to calculate Y, for which the corrections are much smaller.

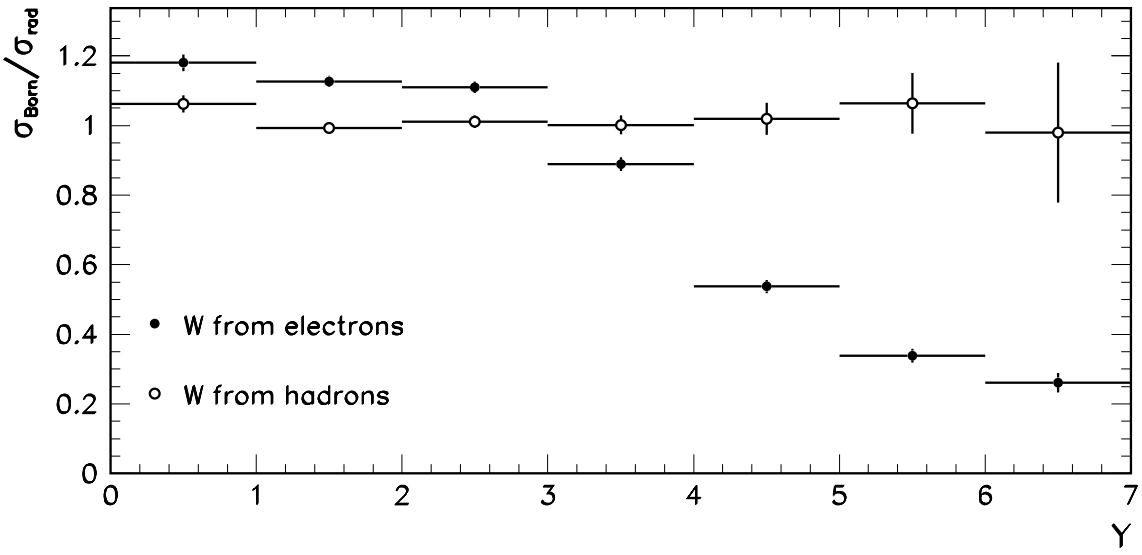

Figure 3: Radiative corrections for the process $e^+e^- \to e^+e^-$ hadrons as a function of Y for two different methods to calculate W: a combined electron/hadronic final state method (electrons), and a pure hadronic final state method (hadrons), as explained in the text.

4 The OPAL detector

A detailed description of the OPAL detector can be found in Ref. [25]. Here only a brief account of the main components relevant to the presented analysis is given.

The central tracking system is located inside a solenoid magnet which provides a uniform axial magnetic field of 0.435 T along the beam axis. The central tracking system consists of a two-layer silicon micro-vertex detector [26], a high precision vertex drift chamber, a large volume jet chamber and a set of z–chambers for accurately measuring track coordinates along the beam direction. The transverse momenta, p_T, of tracks are measured with a precision of $\sigma_{p_T}/p_T = \sqrt{0.02^2 + (0.0015 \cdot p_T)^2}$ (p_T in GeV).

The central detector is surrounded in the barrel region ($|\cos\theta| < 0.82$) by a lead glass electromagnetic calorimeter (ECAL) and a hadronic sampling calorimeter (HCAL). Outside the HCAL, the detector is surrounded by muon chambers. There are similar layers of detectors in the end caps ($0.81 < |\cos\theta| < 0.98$). The barrel and end cap sections of the ECAL are both constructed from lead glass blocks, with a depth of 24.6 radiation lengths in the barrel region and more than 22 radiation lengths in the endcaps.

The small angle region from 47 to 140 mrad around the beam pipe on both sides of the interaction point is covered by the forward detectors (FD) and the region from 25 to 59 mrad by the silicon-tungsten luminometers (SW) [27]. The lower boundary of the SW acceptance is effectively 33 mrad due to the installation of a low-angle shield to shield the

central detector from possible synchrotron radiation.

The FD consists of cylindrical lead-scintillator calorimeters with a depth of 24 radiation lengths divided azimuthally into 16 segments. The electromagnetic energy resolution is approximately $18\%/\sqrt{E}$, where E is in GeV.

The SW detector consists of two cylindrical small angle calorimeters encircling the beam pipe at approximately ± 2.5 m from the interaction point. Each calorimeter is made of a stack of 18 tungsten plates, interleaved with 19 layers of silicon sampling wafers and mounted as two interlocking C–shaped modules around the LEP beam pipe. The depth of the detector amounts to 22 radiation lengths. Each silicon layer consists of 16 wedge-shaped silicon detectors. The sensitive area of the calorimeter fully covers radii between 81 and 142 mm from the beam axis. The energy resolution is approximately 5% on both sides. It is found that the energy resolution hardly varies with the energy due to energy leakage and dead material. In this analysis, the SW detector was used for tagging the scattered electrons from the process $e^+e^- \to e^+e^-$ hadrons.

5 Event selection

The data sample used in this analysis corresponds to an integrated luminosity of 377.7 pb^{-1} accumulated by the OPAL experiment in 1998 (169.3 pb^{-1}) and 1999 (208.4 pb^{-1}) at e^+e^- center-of-mass energies $\sqrt{s_{ee}} = 189 - 202$ GeV with a luminosity weighted average of $\sqrt{s_{ee}}$ = 194 GeV. Double-tagged two-photon events were selected with the following set of cuts:

1. Two electron candidates, one in each SW detector, with energies $E_{1,2} > 0.4E_b$ and polar angles in the range $34 < \theta_{1,2} < 55$ mrad, should be observed. The angles $\theta_{1,2}$ are measured with respect to the original beam direction. On each side the cluster with the highest energy is taken as the electron candidate. The energy threshold for the electron candidates is kept as low as possible in order to access large W values, where BFKL effects may set in.

2. In order to remove events with scattered electrons in FD or in the central detectors, we require that there is no single cluster in these detectors with an energy above $0.25E_b$

3. At least 3 tracks (N_{ch}) have to be found in the tracking system. A track is required to have a minimum transverse momentum of 120 MeV, at least 20 hits in the central jet chamber, and the innermost hit of the track must be within a radius of 60 cm with respect to the z axis. The distance of the point of closest approach to the origin in the $r\phi$ plane must be less than 30 cm in the z direction and less than 2 cm in the $r\phi$ plane. Tracks with a momentum error larger than the momentum itself are rejected if they have less than 80 hits. The number of measured hits in the jet chamber must be more than half of the number of possible hits, where the number of possible hits is calculated from the polar angle θ of the track, assuming that the track has no curvature.

4. The visible invariant mass, $W_{\rm vis}$, is required to be larger than 5 GeV. It is reconstructed from tracks measured in the central tracking detectors, and the position and energy of clusters measured in the electromagnetic and hadronic calorimeters, as well as in the forward detectors FD, excluding clusters assigned to electrons. A matching algorithm [28] is used to avoid double counting of the particle momenta in the calorimeters and tracking chambers.

5. The z position of the primary vertex $|\langle z_0 \rangle|$ is required to be less than 4 cm from the interaction point. Here $\langle z_0 \rangle$ is calculated as the error weighted average of the z coordinates of all tracks at the point of closest approach to the origin in the r, ϕ plane. The requirement that the distance of a single track to the origin of the z axis should be less than 30 cm was not applied in order to keep all possible tracks including those from off-momentum electrons interacting with the beam pipe. This increases the efficiency to reduce the background due to beam–gas interactions. We also require that the distance of the primary vertex from the beam axis should be less than 0.5 cm.

6. In order to ensure that the event is well contained in the detector and to reduce background from beam–gas interactions, the z component of the total momentum vector of the event, $\sum p_z = \Delta p_z$, is required to be less than 35 GeV and that the total energy measured in the event $\sum E$ less $2.2 E_{\rm b}$ where the sum extends over all objects (tracks and clusters) seen in the detector.

7. Remaining Bhabha-like events (i.e. a Bhabha event with random overlap of hadronic activity) are tagged using the back-to-back topology of the scattered electrons, both having an energy larger than $0.7 E_{\rm b}$. Events are rejected if the difference in radius, ΔR and difference in azimuthal angle, $\Delta\phi$ of the position of the two clusters are $\Delta R < 0.5$ cm and $(\pi - 0.1) < |\Delta\phi| < \pi$ rad.

With these cuts 129 events are selected in the data. Among these events, we expect 6.5 and 6.3 background events coming from $\mathrm{e^+e^-}$ background processes for the 1998 and 1999 data samples, respectively. The dominant background stems from the processes $\mathrm{e^+e^- \to e^+e^- \tau\overline{\tau}}$ and $\mathrm{e^+e^- \to e^+e^-e^+e^-}$ and was estimated using the Vermaseren Monte Carlo program [29]. The contribution from other $\mathrm{e^+e^-}$ background, such as $\mathrm{e^+e^- \to q\overline{q}}$ and other processes leading to four fermion final states was found to be negligible, as well as the background from single-tagged two-photon processes, with a cluster from the hadronic final state misidentified as the second electron.

Upstream beam-gas interactions result in off-momentum electrons observed in the SW detectors faking final state electrons from the process $\mathrm{e^+e^- \to e^+e^-}$ hadrons. This background was estimated using a sample of Bhabha events, selected by requiring events with two back-to-back electrons in the SW calorimeters, which each have an energy of more than $0.7 E_{\rm b}$, with $\Delta R < 2.5$ cm and $(\pi - 0.2) < |\Delta\phi| < \pi$ rad. Additional clusters in the SW detectors, which do not belong to the Bhabha event, are counted as off-momentum electrons. The probabilities to have an overlapping off-momentum electron with an event coming from the interaction are determined for the left ($-z$) and right ($+z$) side of the detector separately and amount to 0.00066 (1998, left side), 0.00106 (1998, right side), 0.00139 (1999, left side)

and 0.00280 (1999, right side). The relative statistical precision of these probabilities is 2-3%. Assuming that the overlap probabilities are independent between the left and right side of the detector, using these numbers we predict to find 12.5 events with 'double' overlaps in the Bhabha sample, which agrees well with the 17 observed.

It is essential to check this method to estimate the background on a different process. Here we used a sample of single-tagged two-photon events. The sample is selected with the same cuts as described for the double-tagged selection, except that only one scattered electron is required and cuts 6) and 7) are not applied. The distributions are compared with the absolute prediction for the single-tagged events, using the HERWIG generator with the GRV [30] structure function for the photon, which has been checked to describe the single-tagged cross-section [31] within about 10% for $E > 0.7E_{\rm b}$. The θ, ϕ and energy dependence of the background clusters, as determined from the additional clusters in Bhabha events, is used together with anti-tagged two-photon events generated by PHOJET to artificially create single-tagged events.

Figs. 4 and 5 show the data compared with the prediction resulting from the sum of HERWIG and the background, normalized to the luminosity of the data, for θ, ϕ and energy of the scattered electron. The energy is normalized to the beam energy. Fig. 6 shows the missing longitudinal momentum and missing transverse momentum in the event, calculated including the untagged electron which has been assumed to have zero transverse momentum and an energy equal to the beam energy. Both distributions have been normalized to the beam energy. For energies below $0.6E_{\rm b}$ the off-momentum background clearly dominates and the observed angular dependencies, especially in ϕ, clearly follow the expected shape.

In all, the agreement between data and prediction is very good for all variables, providing confidence that the background from overlap off-momentum beam electrons is under control to a level of about 10%. The off-momentum background estimate was used to calculate the contribution of fake double-tagged events, resulting from the overlap of one background cluster with a single-tag two-photon event and the overlap of two background clusters with an untagged event. In total 3.8 and 14.4 overlap events are predicted for the 1998 and 1999 data samples, respectively. After subtraction of all backgrounds 98 events remain, 32.7 of which are in the 1998 data sample and 65.3 in the 1999 data sample.

The double-tagged events are triggered by two groups of independent triggers. The first trigger is based on the energy deposits of the observed electrons in the SW calorimeters. The second group only relies on the observed tracks and clusters from the hadronic final state. Based on these two independent groups, the trigger efficiency of the hadronic final state alone, for events with two electrons with energies above $0.4E_{\rm b}$, has been determined to be $96 \pm 4\%$, so no correction has been applied.

6 Properties of double-tagged $\gamma^\star\gamma^\star$ events

A PHOJET Monte Carlo sample is used to correct the data for acceptance and resolution effects. It is therefore essential that the shape of all important distributions is well reproduced by the Monte Carlo simulation. In this Section a comparison is made of data distributions with predictions from PHOJET. Variables calculated from the scattered electrons as well as variables calculated from the hadronic final state are studied. The integrated luminosity of the Monte Carlo sample amounts to approximately 40 times that of the data. All Monte Carlo distributions shown in this Section are normalised to the data luminosity. In all plots involving both sides of the SW detector, the sum of the distributions obtained separately for each side is shown.

In Fig. 7 a comparison is made of the data with the sum of the predictions of PHOJET and predicted background, for 1998 and 1999 data samples separately. Shown are the electron energies normalized to the beam energy, the photon virtualities and the visible hadronic invariant mass of the double-tagged events. The variables x and Y are calculated from these quantities, as outlined in Section 2, and are therefore not shown. The shapes of the distributions are well described, but the predictions are generally somewhat below 1999, and above 1998 data. No reason has been found which could explain a difference between 1998 and 1999 data and this difference is therefore attributed to a statistical fluctuation. Since the statistics of this measurement is small, the 1998 and 1999 data will be combined in the following.

In Fig. 8 variables which are based on electron quantities, and $x_{1,2}$, are compared with predictions of PHOJET and background estimates. All variables, the normalized electron energies $E_{1,2}$, the polar angles $\theta_{1,2}$, the azimuthal angles $\phi_{1,2}$, and photon virtualities, are well described by the sum of the signal as predicted by PHOJET and the estimated background from overlaps with off-momentum electrons and other physics processes. A possible exception is the low energy part of the spectrum, where some excess is seen. Note that PHOJET does not contain any effects from BFKL, which would show up exactly in that region. Fig. 8e) shows the logarithm of the ratio of the photon virtualities, $\ln(Q_1^2/Q_2^2)$, of the two photons in an event. This distribution is centered around zero, indicating that the Q^2 values of both photons are generally close to one another, which is needed to test for BFKL effects. The $x_{1,2}$ distribution, shown in Fig. 8f), is calculated using the hadron variables. It agrees well with the data, except for the first bin. This is again the region of large W where BFKL effects may set in.

In Fig. 9 distributions are shown characterizing the hadronic final state in double-tagged two-photon events: the number of tracks, $N_{\rm ch}$, the visible hadronic invariant mass, $W_{\rm vis}$, the hadronic energy, $E_{\rm had}$, the variable Y as well as $\sum p_z$ and $\sum p_T$. Within statistics, the agreement with PHOJET is reasonable, except in the high $W_{\rm vis}$ region where we observe a slight excess over expectation, as expected from the $x_{1,2}$ distribution shown above.

7 Results

The cross-section for the process $e^+e^- \to e^+e^-$ hadrons has been measured in the kinematic region defined by the scattered electron energies $E_{1,2} > 0.4E_b$, the polar angles in the range $34 < \theta_{1,2} < 55$ mrad with respect to the beam direction, and $W > 5$ GeV. From the measurement of the cross-section of $e^+e^- \to e^+e^-$ hadrons we extract the cross-section $\gamma^*\gamma^* \to$ hadrons using $L_{\rm TT}$ (Eq. 9), calculated separately for each bin using Monte Carlo. The $\gamma^*\gamma^* \to$ hadrons cross-sections for the models are calculated using the same $L_{\rm TT}$ factors. The results for $\gamma^*\gamma^* \to$ hadrons are at an average $\langle Q^2 \rangle$ of 17 GeV^2. The cross-sections are presented as a function of x, Q^2, W, and the azimuthal correlation between the two electrons $\Delta\phi$. Here Q^2 refers to the maximum of Q_1^2 and Q_2^2, and x is the corresponding value of x_i. For the comparison with a BFKL calculation we also present the cross-section as a function of Y.

Due to limited statistics in the data, a simple bin-by-bin method was applied to correct for detector and selection inefficiencies. The efficiency, R_e, and purity, R_p, are defined as:

$$R_e = \frac{N^{\rm Det\otimes Had}}{N^{\rm Had}} \qquad R_p = \frac{N^{\rm Det\otimes Had}}{N^{\rm Det}}$$

where $N^{\rm Det\otimes Had}$ is the number of events which are generated in a bin and measured in the same bin, $N^{\rm Had}$ is the number of events which are generated in a bin and $N^{\rm Det}$ is the number of events measured in a bin. In both definitions the terms 'generated' and 'measured' denote events which pass all selection cuts at the hadron or at the detector level, respectively. The correction factor $N^{\rm Had}/N^{\rm Det}$ is obtained by dividing purity by efficiency. For the W variable the purity is typically around 60% over the whole range, and the efficiency is in the range of 30-50%. Similar numbers are obtained for Y and x, while for the $\Delta\phi$ and Q^2 variables the efficiencies are around 60% and purities around 80%. The correction factor is typically around 1.5 and fairly constant.

The total systematic error has been evaluated taking into account several contributions. All changes are applied to the Monte Carlo data samples because of low statistics of the data.

1. The error due to a possible shift of the energy scale of the SW detectors was taken into account by scaling the electron energy by ±1%, in accord with the uncertainty in the scale observed in single-tag events.

2. The error due to a possible mismatch between measured and simulated hadronic energy was taken into account by scaling the hadronic energy by ±3%.

3. To estimate the uncertainties due to the selection cuts, we have performed the following checks:

   (a) The lower cut on $\theta_{1,2}$ was changed from 34 mrad by ±0.4 mrad.

(b) The lower cut on $E_{1,2}$ was changed by $\pm 5\%$.

(c) The cut on W was changed by ± 0.5 GeV.

(d) The cut on $|\langle z_0 \rangle|$ was changed by ± 1.0 cm

(e) The cut on the distance of the primary vertex to the beam axis was changed by ± 0.1 cm.

4. The PYTHIA Monte Carlo was used to correct the data, instead of PHOJET. The differences between the models are generally within 10-15%, except for the high W region where the difference amounts to 25%. The differences were taken as the error.

5. In modelling the region of $W < 5$ GeV PHOJET is incomplete. This affects the measurement only through migrations from lower to higher W. In order to estimate the influence of that region in PHOJET, the number of events with $W < 5$ GeV was scaled by $\pm 50\%$.

6. The uncertainty in the estimation of the off-momentum background was taken to be 10% of the background.

The main contribution to the systematic errors comes from varying the lower cuts on $\theta_{1,2}$ and W. The normalisation uncertainty due to the luminosity measurement is less than 1% and has been neglected.

The total measured cross-section for the process $e^+e^- \to e^+e^-$ hadrons in the previously defined phase space, is 0.40 ± 0.05 (stat) ± 0.05 (sys) pb. The expected cross-section from PHOJET is 0.39 ± 0.02 (stat) pb, while the prediction for QPM is 0.27 ± 0.02 (stat) pb.

In Fig. 10 we show the measured cross-sections for the processes $e^+e^- \to e^+e^-$ hadrons and $\gamma^*\gamma^* \to$ hadrons as a function of x and Q^2. The numerical values of the cross-sections are given in Tables 1 and 2. PHOJET generally describes the data while the QPM prediction is too low. Fig. 11 shows the measured cross-sections as a function of W and $\Delta\phi$, the difference in azimuthal angle between the two electrons in the laboratory reference frame. The model predictions are generally below the data for W values larger than 20 GeV. Studies for HERA have shown [32] that angular variables similar to $\Delta\phi$ can be sensitive to the presence of BFKL dynamics, but so far no calculations are available for $\gamma^*\gamma^*$ scattering. The data show that the distribution of $\Delta\phi$ is flat. PHOJET does not describe the $\Delta\phi$ distribution whereas QPM reproduces the shape of the distribution well.

In Fig. 12 we compare the measured cross-section for the processes $e^+e^- \to e^+e^-$ hadrons and $\gamma^*\gamma^* \to$ hadrons as a function of Y, with the PHOJET Monte Carlo, the QPM calculation and numerical BFKL calculations (Tables 1 and 2). The BFKL predictions are shown for the LO calculation [33], a NLO calculation [34] and a (partial) HO calculation [35]. All BFKL predictions are shown for $Y > 2$, except for the NLO calculation which has been calculated for $Y > 1$. For the data the Y variable is calculated as $Y = \ln(W^2/\sqrt{Q_1^2 Q_2^2})$, with W calculated from the hadronic final state. The QPM prediction is systematically below the data for $Y > 2$. The PHOJET model, which does not include BFKL-like effects, gives

a good description of the data, with the possible exception of the highest Y values. In the region $Y > 2$ the $\gamma^*\gamma^* \to$ hadrons measured cross-section is 0.221 ± 0.039 pb with 0.165 pb (PHOJET) and 0.112 pb (QPM) expected.

The BFKL predictions can be calculated only large values of Y For all BFKL predictions shown the cross-section is significantly larger than the PHOJET prediction for $Y > 3$, and the differences increase with increasing Y. The LO BFKL calculation predicts a cross-section which is too large compared to the data. This LO BFKL calculation (Bartels99) [33] already incorporates improvements compared to the original results [10] by including effects of the charm quark mass, the running of the strong coupling constant α_s and contribution of longitudinal photon polarization states. Hence BFKL effects as large as predicted by the LO calculations are not confirmed by the data. BFKL cross-sections have been calculated to NLO (Kim99) [34], using the so-called BLM [36] optimal scale setting. At the highest Y value the NLO-BFKL cross-section is a factor seven larger than the PHOJET prediction. The data lies in between these two predictions. Finally, the calculation (Kwiecinski) [35] contains the dominant contribution of the higher order corrections via the so called consistency constraint, to all orders. Its prediction in the highest reachable Y range is about a factor two lower than for the NLO calculation, and agrees with the data in the full range.

In short, the LO BFKL cross-sections are too large, however the higher order calculations, which predict smaller BFKL effects, are close to the measurements. The measurements lie in between the predictions with and without BFKL effects, but limited statistics precludes firmer conclusions.

8 Summary and conclusions

A data sample collected by the OPAL experiment at LEP based on an integrated luminosity of 377.7 pb^{-1} and for e^+e^- centre-of-mass energies $\sqrt{s_{ee}} = 189 - 202$ GeV has been used to study interactions of virtual photons. Differential cross-sections are measured as functions of x, Q^2, W, $\Delta\phi$ and Y. At large W the measured cross-sections are larger than the QPM predictions, which shows that the contributions of additional processes to the cross-section are important. PHOJET describes reasonably well the x, Q^2, W, and Y distributions but has a different shape for $\Delta\phi$. A slight excess in the data over the PHOJET prediction is seen at the highest Y values reached, in the region where the onset of BFKL effects may be expected. Within current calculations these effects could lead to an increase of the cross-section by a factor up to 20 for the largest Y values. The data rule out BFKL cross-sections as predicted by LO calculations. Calculations including higher order corrections are consistent with the measured cross-sections, but the limited statistics of the data prevents establishing the onset of BFKL dynamics in this reaction.

References

[1] OPAL Collaboration, G. Abbiendi et al., Eur. Phys. J. **C14** (2000) 199.

[2] OPAL Collaboration, G. Abbiendi et al., Eur. Phys. J. **C10** (1999) 547.

[3] OPAL Collaboration, G. Abbiendi et al., Eur. Phys. J. **C11** (1999) 409.

[4] OPAL Collaboration, K. Ackerstaff et al., Phys. Lett. **B412** (1997) 225.

[5] OPAL Collaboration, K. Ackerstaff et al., Phys. Lett. **B411** (1997) 387.

[6] OPAL Collaboration, K. Ackerstaff et al., Z. Phys. **C74** (1997) 33.

[7] R. Engel, Z. Phys. **C66** (1995) 203;
R. Engel and J. Ranft, Phys. Rev. **D54** (1996) 4246.

[8] E.A. Kuraev, L.N. Lipatov and V.S. Fadin, Sov. Phys. JETP **45** (1977) 199;
Ia. Balitski and L.N. Lipatov, Sov. J. Nucl. Phys. **28** (1978) 822.

[9] L3 Collaboration, M.Acciarri et al., Phys. Lett. **B453** (1999) 333.

[10] J. Bartels, A. De Roeck and H. Lotter, Phys. Lett. **B389** (1996) 742;
J. Bartels, A. De Roeck, H. Lotter and C. Ewerz, DESY preprint 97-123E, *The $\gamma^*\gamma^*$ Total Cross-Section and the BFKL pomeron at the 500 GeV e^+e^- Linear Collider*, hep-ph/9710500;
S.J. Brodsky, F. Hautmann and D.E. Soper, Phys. Rev. **D56** (1997) 6957.

[11] V.M. Budnev, I.F. Ginzburg, G.V. Meledin and V.G. Serbo, Phys. Rep. **15** (1975) 181.

[12] R. Nisius, Phys. Rep. **332** (2000) 165.

[13] ZEUS Collaboration, J. Breitweg et al., Eur. Phys. J. **C6** (1999) 239;
H1 Collaboration, C. Adloff et al., Nucl. Phys. **B538** (1999) 3;
H1 Collaboration, C. Adloff et al., Phys. Lett. **B462** (1999) 440.

[14] S.J. Brodsky, F. Hautmann and D.E. Soper, Phys. Rev. Lett. **78** (1997) 803.

[15] A. Białas, W. Czyż and W. Florkowski, Eur. Phys. J. **C2** (1998) 683.

[16] M. Boonekamp, A. De Roeck, C. Royon and S. Wallon, Nucl. Phys. **B555** (1999) 540.

[17] G. Altarelli and G. Parisi, Nucl. Phys. **B126** (1977) 298;
V.N. Gribov and L.N. Lipatov, Sov. J. Nucl. Phys. **15** (1972) 438;
L.N. Lipatov, Sov. J. Nucl. Phys. **20** (1975) 96;
Y.L. Dokshitzer, Sov. Phys. JETP. **46** (1977) 641.

[18] I.F. Ginzburg and V.G. Serbo, Phys. Lett. **B109** (1982) 231.

[19] T. Sjöstrand, Comp. Phys. Comm. **82** (1994) 74;
T. Sjöstrand, LUND University Report, LU-TP-95-20 (1995).

[20] C. Friberg and T. Sjöstrand, *Total Cross Sections and Event Properties from Real to Virtual Photons* LUND University Report, LU-TP-00-29 (2000), hep-ph/0007314.

[21] G. Marchesini et al., Comp. Phys. Comm. **67** (1992) 465.

[22] The LEP Working Group for Two-Photon Physics, ALEPH, L3 and OPAL Collaborations, *Comparison of Deep Inelastic Electron-Photon Scattering Data with the Herwig and Phojet Monte Carlo Models*, CERN-EP-2000-109, Submitted to Eur. Phys. J. C.

[23] G.A. Schuler, Comp. Phys. Comm. **108** (1998) 279.

[24] F.A. Berends, P.H. Daverveldt and R. Kleiss, Nucl. Phys. **B253** (1985) 421; Comp. Phys. Comm. **40** (1986) 271; Comp. Phys. Comm. **40** (1986) 285; Nucl. Phys. **B264** (1986) 243.

[25] OPAL Collaboration, K.Ahmet et al., Nucl. Instr. Meth. **A305** (1991) 275.

[26] P.P. Allport et al., Nucl. Instr. Meth. **A324** (1993) 34.

[27] M. Hauschild et al., Nucl. Instr. Meth. **A379** (1996) 436.

[28] OPAL Collaboration, G. Alexander et al., Phys. Lett. **B377** (1996) 181.

[29] J.A.M. Vermaseren, Nucl. Phys. **B229** (1983) 347.

[30] M. Glück, E. Reya and A. Vogt, Phys. Rev. **D45** (1992) 3986;
M. Glück, E. Reya and A. Vogt, Phys. Rev. **D46** (1992) 1973.

[31] The OPAL Collaboration, G. Abbiendi et al, *Measurement of the low-x behaviour of the photon structure function* F_2^γ, CERN-EP-2000-082, Submitted to Eur. Phys. J. C.

[32] J. Bartels, V. Del Duca and M. Wüsthoff, Z. Phys. **C76** (1997) 75.

[33] J. Bartels, C. Ewerz and R. Staritzbichler, *Effects of the Charm Quark Mass on the BFKL* $\gamma^*\gamma^*$ *Total Cross Section at LEP*, hep-ph/0004029.

[34] S.J. Brodsky et al., JETP Lett. **70** (1999) 155;
V. Kim, private communication.

[35] J. Kwiecinski and L. Motyka, Phys. Lett. **B462** (1999) 203.

[36] S.J. Brodsky, G.P. Lepage and P.B. Mackenzie, Phys. Rev. **D28** (1983) 228.

$\langle x \rangle$	range	$N_{\rm ev}$	$\frac{d\sigma}{dx}$ OPAL [pb]	Statistical error	Systematic error		$\frac{d\sigma}{dx}$ PHOJET [pb]
					up	down	
0.06	0. - 0.1	38.2	1.88	0.37	0.15	0.31	1.33
0.15	0.1 - 0.2	38.6	1.51	0.27	0.10	0.18	1.27
0.26	0.2 - 0.35	22.5	0.55	0.13	0.11	0.17	0.83

$\langle Q^2 \rangle$ [GeV^2]	range [GeV^2]	$N_{\rm ev}$	$\frac{d\sigma}{dQ^2}$ OPAL [pb/GeV^2]	Statistical error	Systematic error		$\frac{d\sigma}{dQ^2}$ PHOJET [pb/GeV^2]
					up	down	
13.6	10 - 16	31.4	0.024	0.005	0.004	0.003	0.021
18.9	16 - 22	42.7	0.029	0.005	0.003	0.004	0.027
24.4	22 - 28	17.1	0.011	0.003	0.001	0.003	0.016

$\langle W \rangle$ [GeV]	range [GeV]	$N_{\rm ev}$	$\frac{d\sigma}{dW}$ OPAL [pb/GeV]	Statistical error	Systematic error		$\frac{d\sigma}{dW}$ PHOJET [pb/GeV]
					up	down	
7.2	5 - 10	44.6	0.033	0.006	0.0056	0.0074	0.041
12.4	10 - 15	22.1	0.019	0.005	0.0013	0.0013	0.021
20.6	15 - 35	26.6	0.006	0.001	0.0004	0.0013	0.004
41.5	35 - 50	4.2	0.002	0.001	0.0002	0.0004	0.000

$\Delta\phi$	range	$N_{\rm ev}$	$\frac{d\sigma}{d\Delta\phi}$ OPAL [pb]	Statistical error	Systematic error		$\frac{d\sigma}{d\Delta\phi}$ PHOJET [pb]
					up	down	
2.83	-3.14 - -2.51	21.9	0.149	0.037	0.010	0.012	0.068
2.20	-2.51 - -1.89	18.5	0.125	0.034	0.011	0.022	0.084
1.57	-1.89 - -1.26	25.1	0.166	0.037	0.015	0.024	0.121
0.94	-1.26 - -0.63	16.9	0.110	0.031	0.013	0.018	0.164
0.31	-0.63 - 0.00	15.5	0.098	0.029	0.012	0.020	0.191

Y	range	$N_{\rm ev}$	$\frac{d\sigma}{dY}$ OPAL [pb]	Statistical error	Systematic error		$\frac{d\sigma}{dY}$ PHOJET [pb]
					up	down	
0.5	0 - 1	15.0	0.055	0.016	0.030	0.020	0.079
1.5	1 - 2	32.4	0.118	0.024	0.009	0.024	0.141
2.5	2 - 3	27.2	0.123	0.028	0.010	0.011	0.114
3.5	3 - 4	14.8	0.070	0.021	0.006	0.015	0.041
5.0	4 - 6	7.1	0.028	0.013	0.002	0.012	0.010

Table 1: The cross-section for the process $e^+e^- \to e^+e^-$ hadrons in the region $E_{1,2} > 0.4E_{\rm b}$, $34 < \theta_{1,2} < 55$ mrad and $W > 5$ GeV, as a function of x, Q^2, W, $\Delta\phi$ and Y. The average value of each quantity in a bin, the bin boundaries, number of measured events in the bin after background subtraction, value of the cross-section with statistical and systematic errors as well as the cross-section predicted by PHOJET1.10, are given.

$\langle x \rangle$	$\frac{d\sigma}{dx}$ OPAL [nb]	Statistical error	Systematic error up	Systematic error down	$\frac{d\sigma}{dx}$ PHOJET [nb]	$\frac{d\sigma}{dx}$ QPM [nb]	L_{TT} 10^{-3}
0.06	60.08	11.66	3.55	3.91	42.36	28.94	0.0314
0.15	110.26	19.83	4.60	4.87	92.96	64.55	0.0137
0.26	39.64	9.46	3.52	3.95	59.72	41.67	0.0139

$\langle Q^2 \rangle$ [GeV^2]	$\frac{d\sigma}{dQ^2}$ OPAL [nb/GeV^2]	Statistical error	Systematic error up	Systematic error down	$\frac{d\sigma}{dQ^2}$ PHOJET [nb/GeV^2]	$\frac{d\sigma}{dQ^2}$ QPM [nb/GeV^2]	L_{TT} 10^{-3}
13.6	1.24	0.27	0.57	0.56	1.08	0.80	0.0191
18.9	1.19	0.20	0.47	0.51	1.12	0.75	0.0244
24.4	0.76	0.21	0.48	0.55	1.12	0.73	0.0147

$\langle W \rangle$ [GeV]	$\frac{d\sigma}{dW}$ OPAL [nb/GeV]	Statistical error	Systematic error up	Systematic error down	$\frac{d\sigma}{dW}$ PHOJET [nb/GeV]	$\frac{d\sigma}{dW}$ QPM [nb/GeV]	L_{TT} 10^{-3}
7.2	1.47	0.25	0.60	0.64	1.82	1.30	0.0226
12.4	1.63	0.41	0.65	0.65	1.83	1.10	0.0116
20.6	0.36	0.08	0.29	0.33	0.20	0.15	0.0180
41.5	0.45	0.25	0.50	0.51	0.10	0.09	0.0044

$\Delta\phi$	$\frac{d\sigma}{d\Delta\phi}$ OPAL [nb]	Statistical error	Systematic error up	Systematic error down	$\frac{d\sigma}{d\Delta\phi}$ PHOJET [nb]	$\frac{d\sigma}{d\Delta\phi}$QPM [nb]	L_{TT} 10^{-3}
2.83	17.29	4.31	2.11	2.13	7.93	10.54	0.0086
2.20	12.78	3.51	1.92	2.03	8.57	9.71	0.0098
1.57	14.02	3.14	1.84	1.93	10.26	7.77	0.0118
0.94	7.66	2.19	1.54	1.59	11.45	5.80	0.0143
0.31	6.20	1.85	1.42	1.50	12.11	4.66	0.0158

Y	$\frac{d\sigma}{dY}$ OPAL [nb]	Statistical error	Systematic error up	Systematic error down	$\frac{d\sigma}{dY}$ PHOJET [nb]	$\frac{d\sigma}{dY}$ QPM [nb]	L_{TT} 10^{-3}
0.5	6.11	1.81	1.94	1.68	8.69	5.56	0.0091
1.5	7.66	1.53	1.28	1.48	9.16	6.82	0.0154
2.5	9.17	2.04	1.47	1.48	8.45	5.15	0.0135
3.5	6.65	2.04	1.46	1.57	3.89	3.09	0.0105
4.5	2.65	1.26	1.13	1.29	0.92	0.73	0.0105

Table 2: The cross-section for the process $\gamma^\star\gamma^\star \to$ hadrons at $\langle Q^2 \rangle = 17$ GeV^2 as a function of x, Q^2, W, $\Delta\phi$ and Y. The average value of each quantity in a bin, value of the cross-section with statistical and systematic errors, the cross-section predicted by PHOJET1.10 and QPM as well as L_{TT} are given.

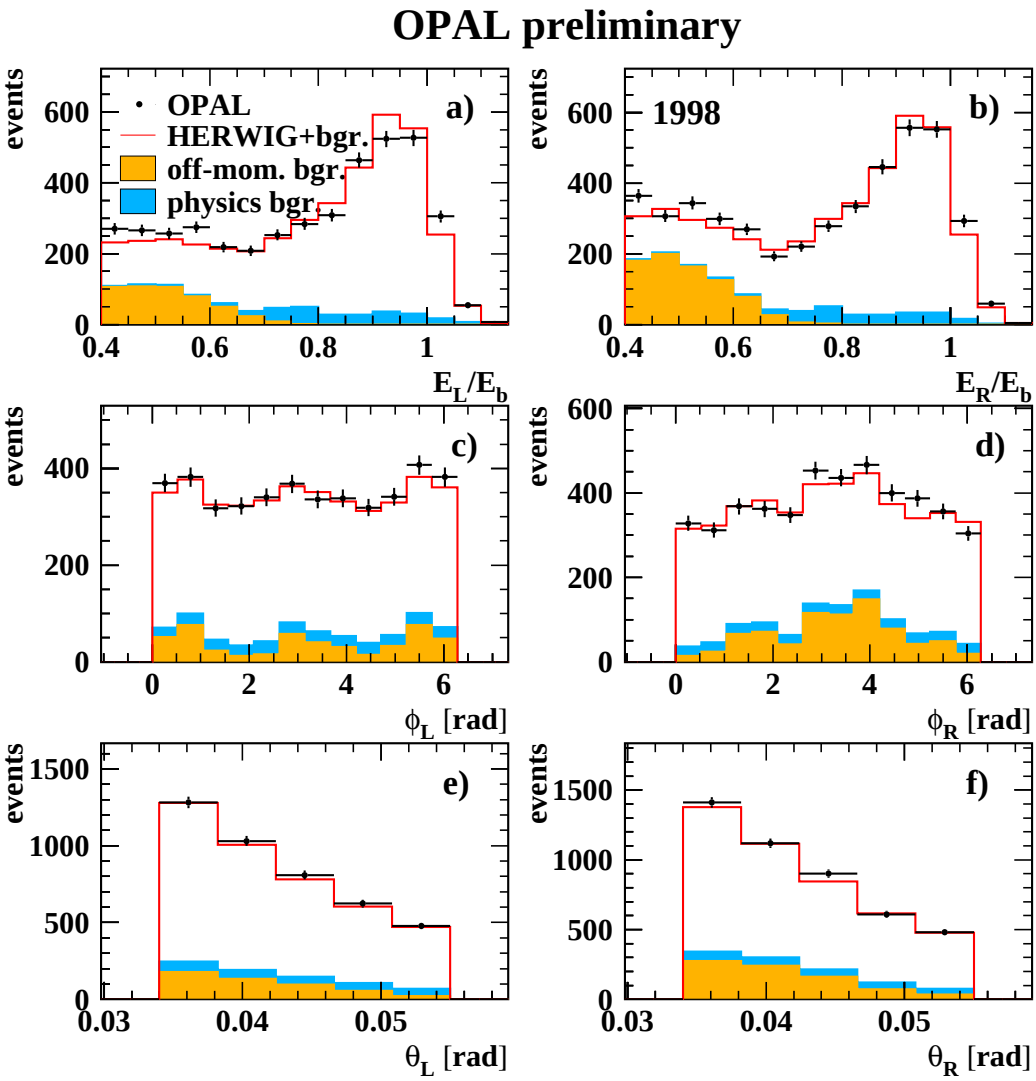

Figure 4: Distributions of the electron energy normalized to the beam energy (a,b), electron azimuthal angle (c,d), and electron polar angle (e,f), shown separately for the left and right side of the OPAL detector, for selected single-tag two-photon events in 1998. The histograms are the predictions for the single-tag two-photon process from HERWIG, the off-momentum background contribution, and the background from other physics channels.

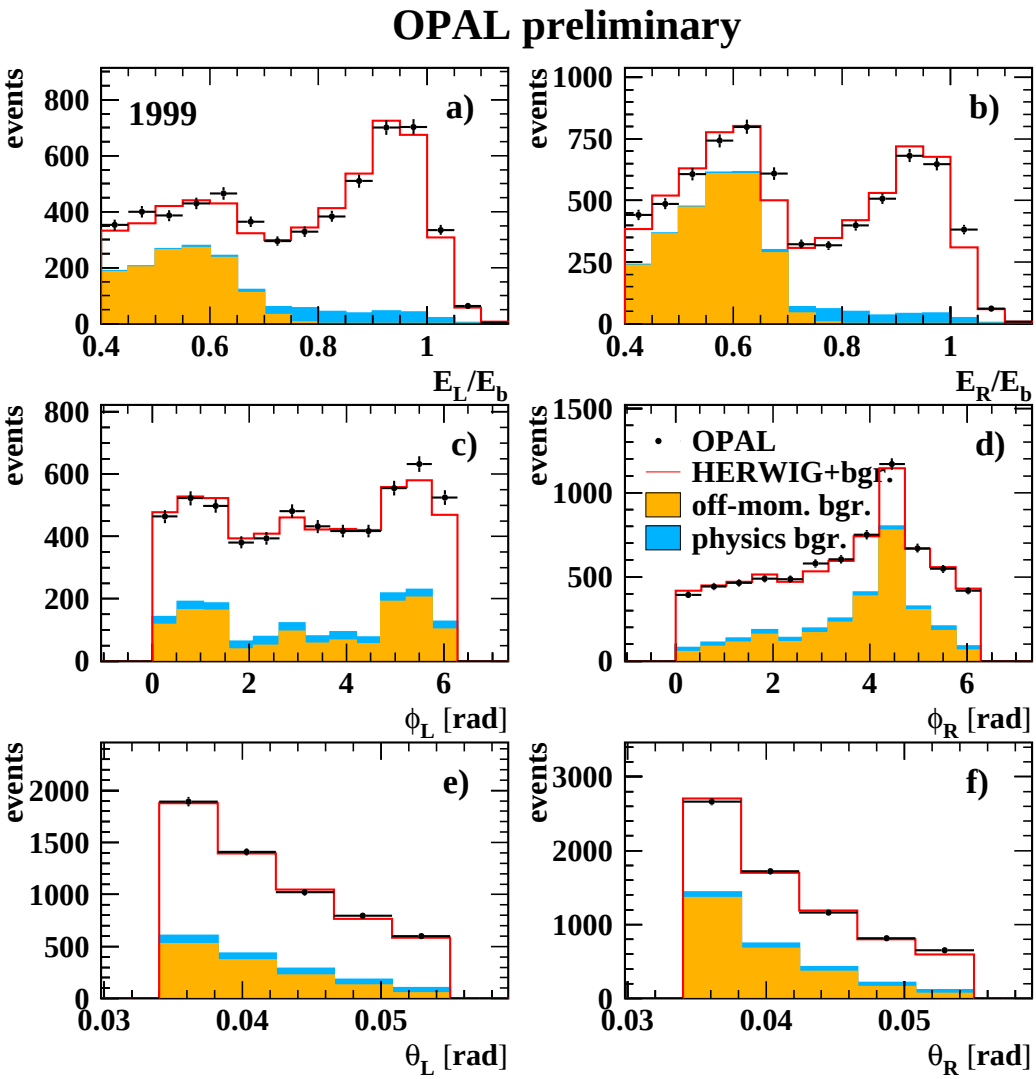

Figure 5: Distributions of the electron energy normalized to the beam energy (a,b), electron azimuthal angle (c,d), and electron polar angle (e,f), shown separately for the left and right side of the OPAL detector, for selected single-tag two-photon events in 1999. Backgrounds as in Fig. 4

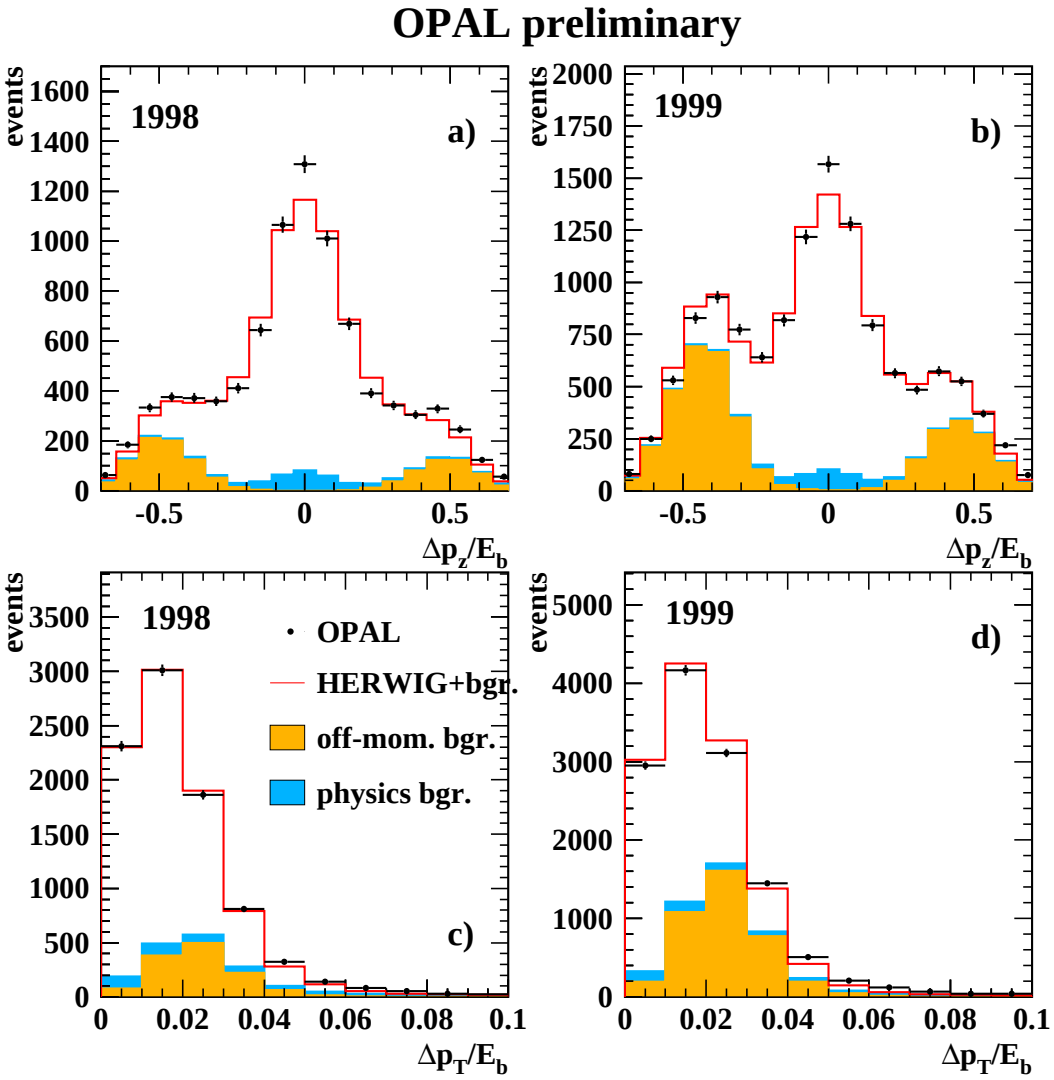

Figure 6: Distributions of the scaled missing longitudinal momentum (a,b) and the scaled missing transverse momentum (c,d) in single-tag events. Backgrounds as in Fig. 4.

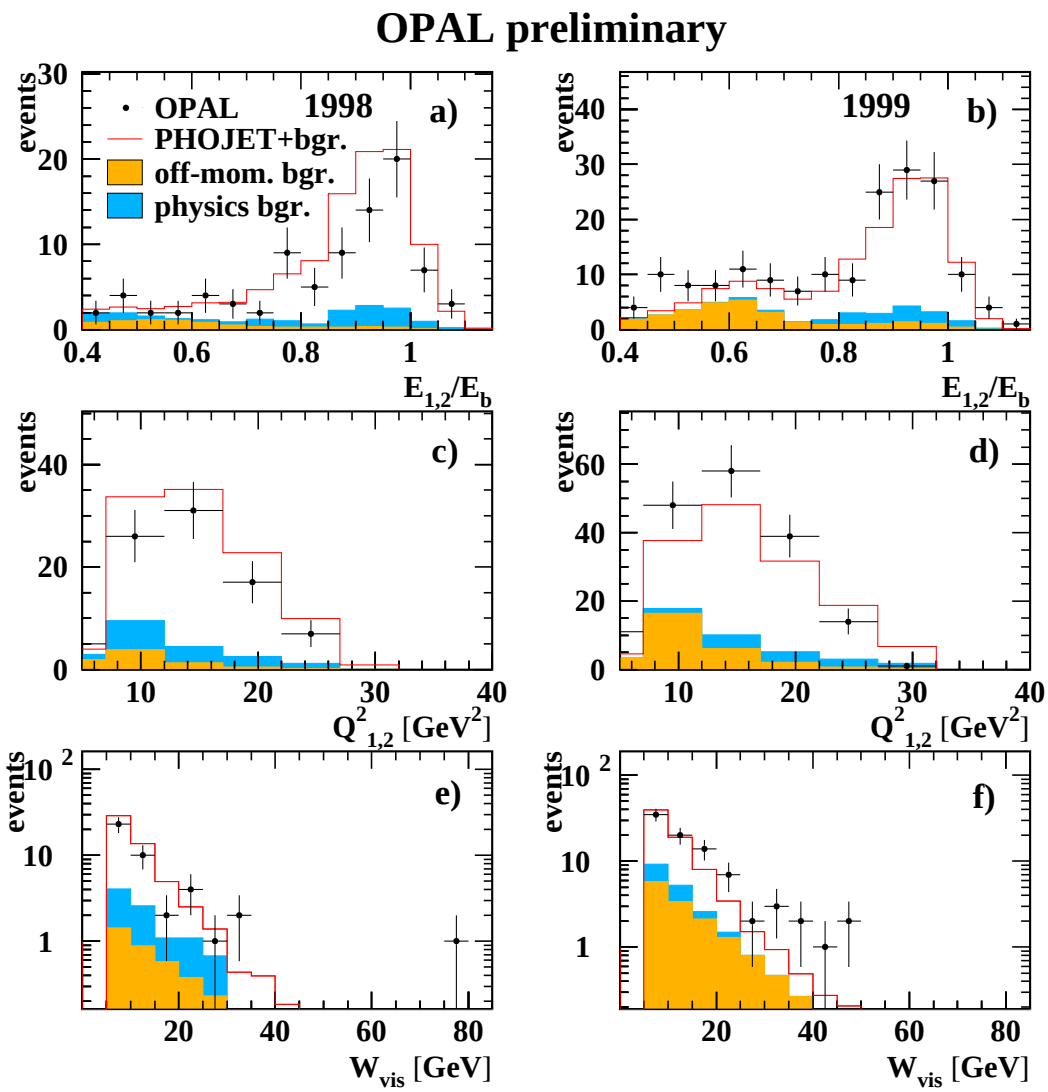

Figure 7: Distributions of the energy of the electrons, normalized to the beam energy (a,b), the virtuality of both photons (c,d) and the hadronic invariant mass of the double-tagged events (e,f), for the 1998 and 1999 data samples. The histograms are the predictions of the double-tagged two-photon process from PHOJET, the off-momentum background contribution, and the background from other physics channels.

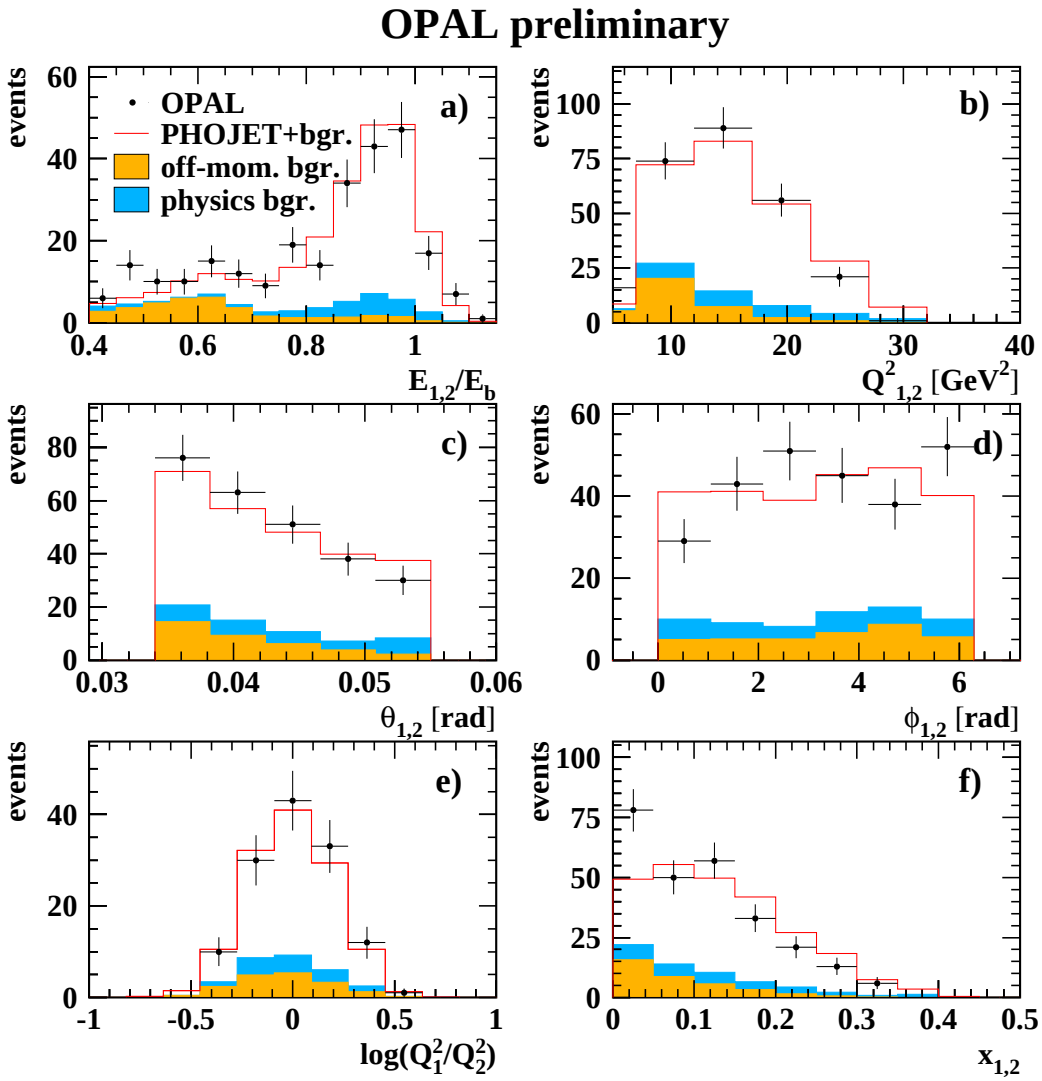

Figure 8: Distributions of (a) the energy of the electrons, normalized to the beam energy, (b) the virtuality of both photons and (c) the polar angle of the electrons, (d) the azimuthal angle of the electrons, (e) the ratio of the photon virtualities of double-tagged two-photon events, and (f) the x values, PHOJET predictions and backgrounds as in Fig. 7.

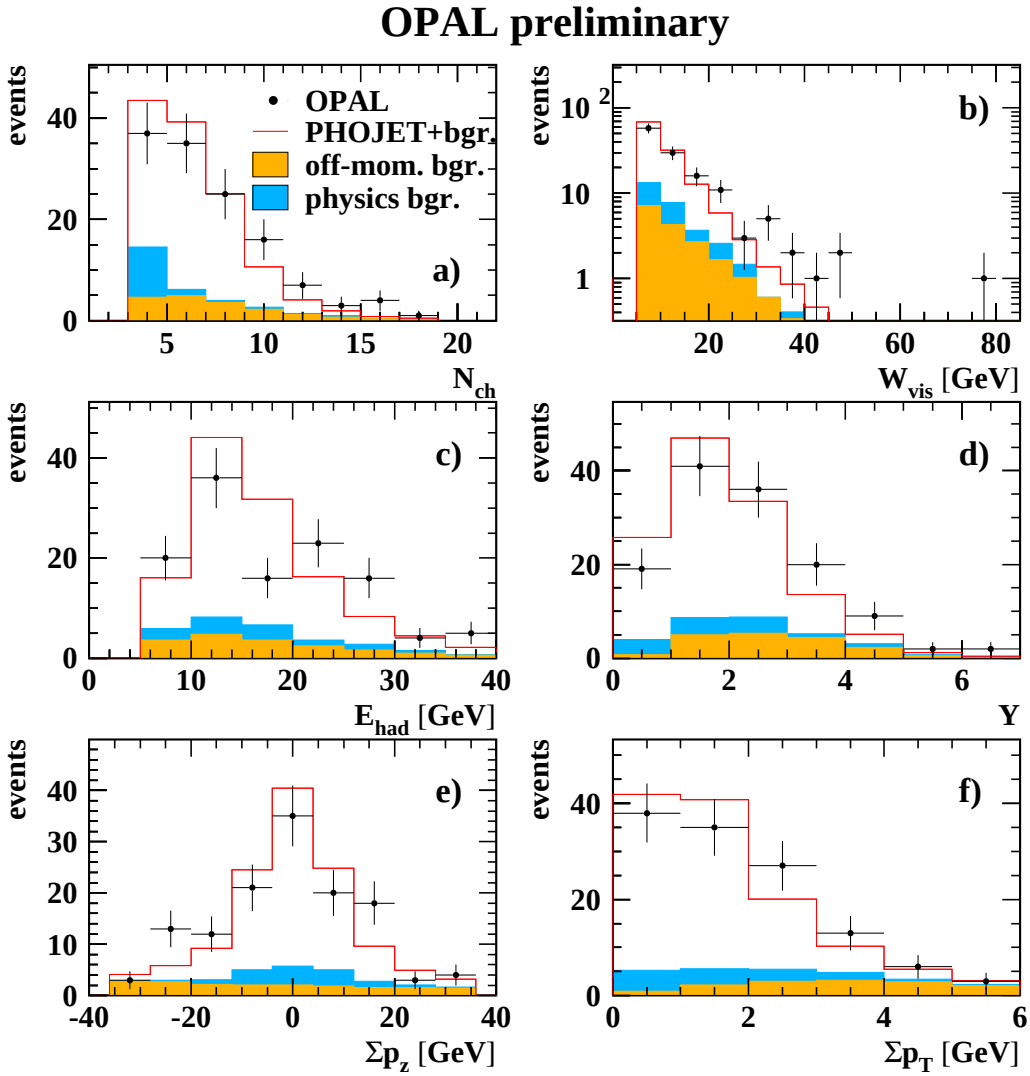

Figure 9: Distributions of (a) the number of tracks of the hadronic final state, (b) the hadronic invariant mass, (c) the total hadronic energy (d) the variable Y, (e) the missing longitudinal momentum and (f) the missing transverse momentum for double-tagged events. PHOJET predictions and backgrounds as in Fig. 7.

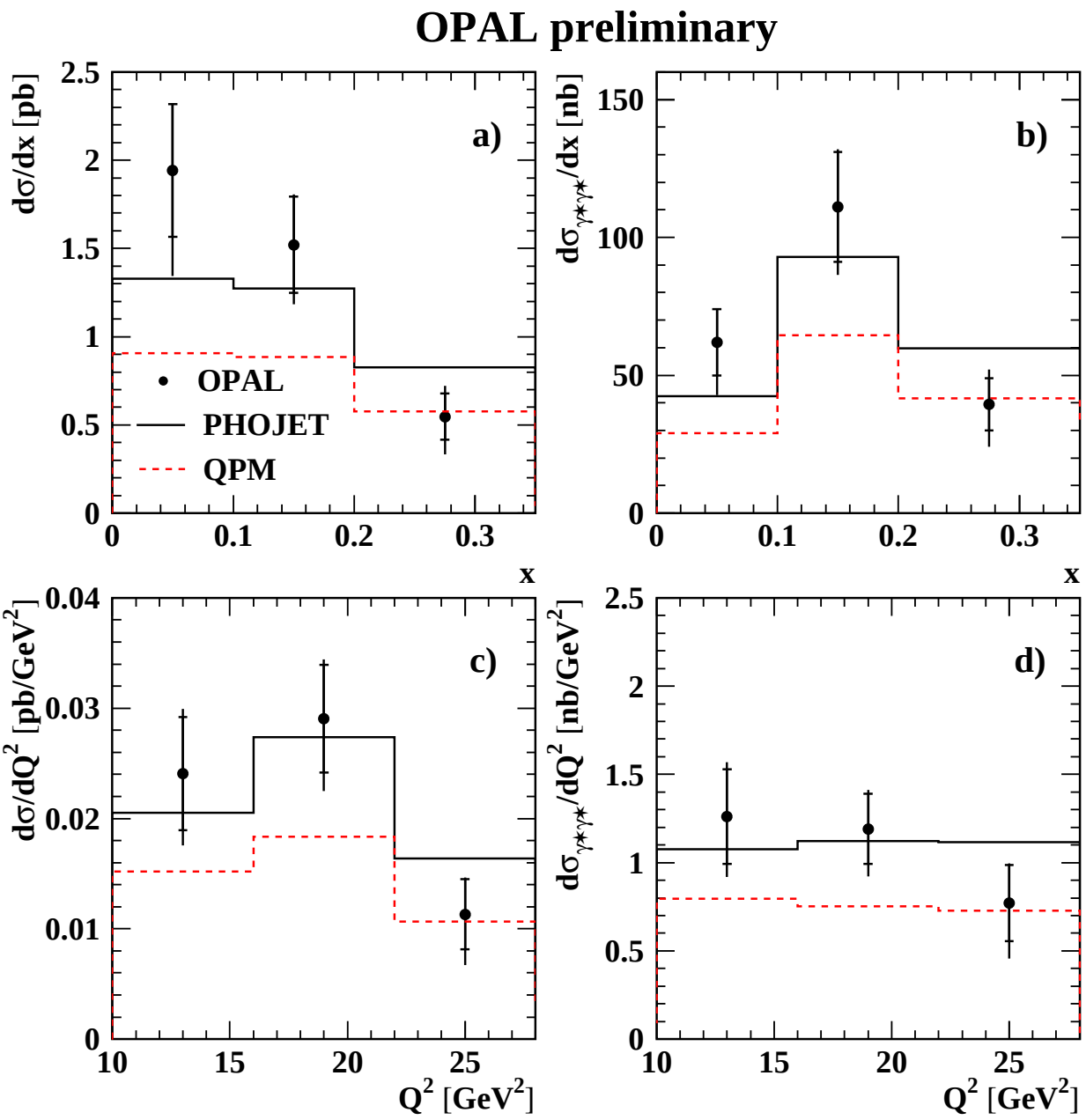

Figure 10: Cross-sections for the process $e^+e^- \to e^+e^-$ hadrons in the region $E_{1,2} > 0.4E_b$, $34 < \theta_{1,2} < 55$ mrad and $W > 5$ GeV, and for the process $\gamma^*\gamma^* \to$ hadrons for $\langle Q^2 \rangle = 17$ GeV^2, as functions of x (a,b) and Q^2 (c,d). Data are shown as full dots in the center of the bins. The inner error bars represent the statistical errors and the outer error bars represent statistical and systematic errors added in quadrature. Predictions of PHOJET are shown as solid lines, and those of QPM as dashed lines.

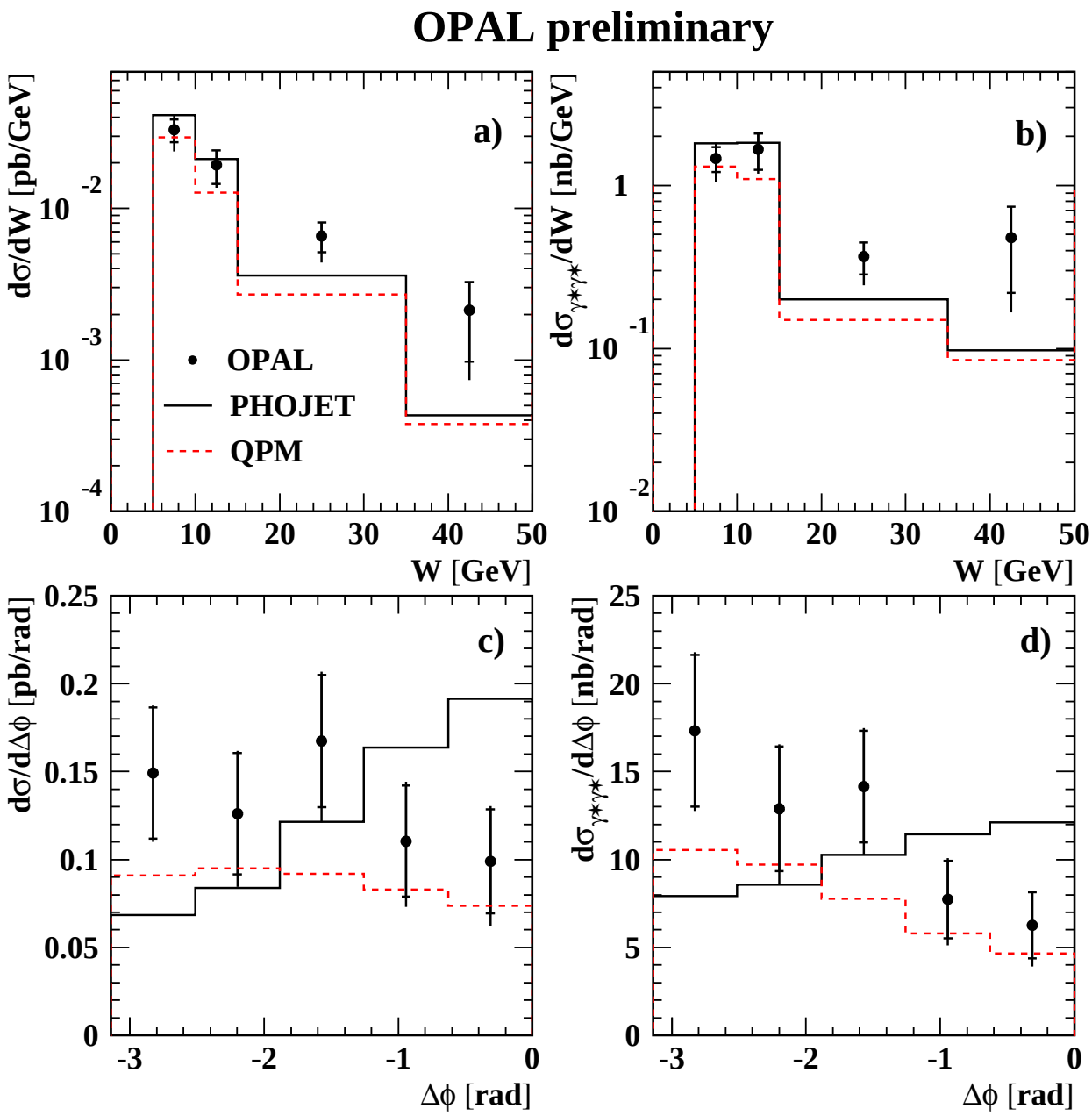

Figure 11: Cross-sections for the process $e^+e^- \to e^+e^-$ hadrons in the region $E_{1,2} > 0.4E_b$, $34 < \theta_{1,2} < 55$ mrad and $W > 5$ GeV, and for the process $\gamma^*\gamma^* \to$ hadrons for $\langle Q^2 \rangle = 17$ GeV^2, as functions of W (a,b) and $\Delta\phi$ (c,d). Data are shown as full dots in the center of the bins. The inner error bars represent the statistical errors and the outer error bars represent statistical and systematic errors added in quadrature. Predictions of PHOJET are shown as solid lines, and those of QPM as dashed lines.

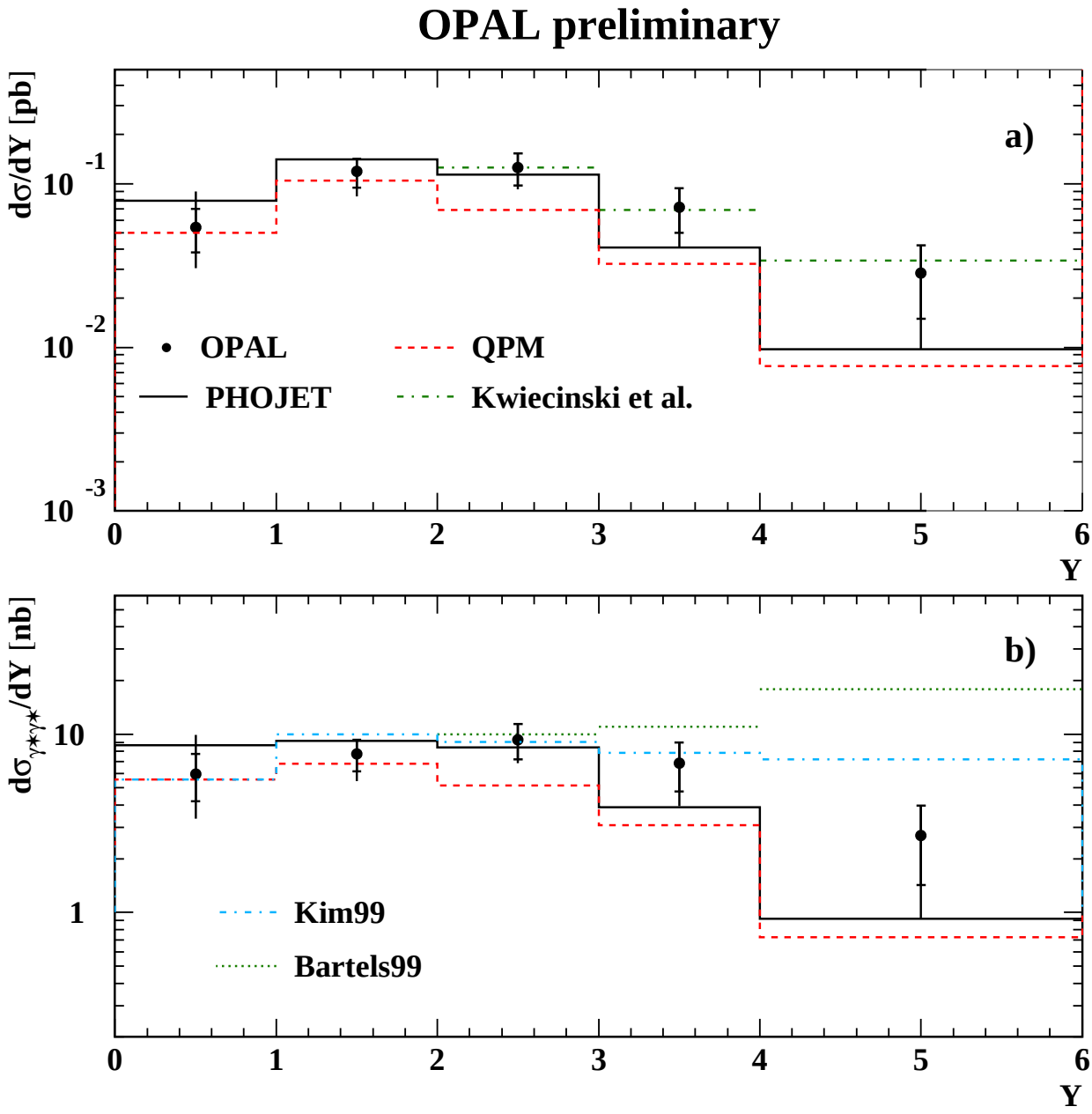

Figure 12: Cross-sections for the process $e^+e^- \to e^+e^-$ hadrons in the region $E_{1,2} > 0.4E_b$, $34 < \theta_{1,2} < 55$ mrad and $W > 5$ GeV, and the process $\gamma^*\gamma^* \to$ hadrons for $\langle Q^2 \rangle = 17$ GeV^2, as a function of Y. Data are shown as full dots in the center of the bins. The inner error bars represent the statistical errors and the outer error bars represent statistical and systematic errors added in quadrature. Predictions of PHOJET are shown as the solid lines, and those of QPM as dashed lines. Three BFKL calculations are shown: a LO one from Bartels et al. (Bartels99), NLO from Kim et al. (Kim99) and the calculation from Kwiecinski et al., using the consistency constraint.